JOM, Vol. 75, No. 9, 2023
https://doi.org/10.1007/s11837-023-05934-z

TECHNICAL ARTICLE

Microstructural Evolution and Mechanical Behaviour of Near-Eutectic High Entropy Alloy

RAHUL JOHN ,[1,2] K. GURUVIDYATHRI,[3] B.S. MURTY,[2,4] and DANIEL FABIJANIC[1,5]

1.—Institute for Frontier Materials, Deakin University, Geelong, VIC 3220, Australia. 2.—Department of Metallurgical and Materials Engineering, Indian Institute of Technology Madras, Chennai 600036, India. 3.—School of Engineering Sciences and Technology, University of Hyderabad, Gachibowli, Hyderabad 502285, India. 4.—Department of Material Science and Metallurgical Engineering, Indian Institute of Technology Hyderabad, Kandi, Sangareddy, Telangana 502284, India. 5.—e-mail: daniel.fabijanic@deakin.edu.au

In the current work, the thermal stability of the eutectic regions and precipitation and mechanical behaviour of near eutectic high-entropy alloy is studied. The alloy solidified as FCC and underwent sequential ordering to $L1_2$ with order–disorder transition temperature between 700°C and 1000°C. Cooling rate, variation in the concentration boundary layer, thermal gradient and interfacial energy were attributed to define the eutectic morphology ($L1_2$ and B2). Thermal exposure resulted in homogeneous precipitation of acicular Al-Ni-rich B2 phase within the proeutectic and irregular eutectic regions. The preferential B2 precipitation within the irregular eutectic regions was attributed to the lower stability and higher lattice strain associated with these regions. The FCC: B2 phase fraction after heat treatment was similar to that of the eutectic alloy. Furthermore, lamellar degradation, globularization and Ostwald ripening of the B2 phase were observed after heat treatment. Lamellar degradation occurred via mechanisms like cylinderization, edge spheroidization, termination migration and boundary splitting. The experimental observations on the phase evolution, stability and order–disorder transformation matched well with the CALPHAD predictions except for the σ phase formation. B2 precipitation during heat treatment enhanced the mechanical behaviour of the alloy. However, the work hardening rate was superior for as-cast alloy.

INTRODUCTION

High-entropy alloys (HEAs) containing concentrated multi-component compositions are extensively studied because of their interesting properties.[1,2] Among the various HEAs, eutectic HEAs possess superior strength-ductility combinations.[3–6] One of the widely researched eutectic HEAs is $AlCoCrFeNi_{2.1}$ (henceforth referred to as the eutectic alloy). The alloy in as-cast condition exhibited lamellar $L1_2$ and B2 phases in 65:35 vol.%.[3] The $L1_2$ phase was found to be Co-Cr-Fe-rich, while B2 was rich in Al and Ni.[7,8] The lamellar regions of the alloy displayed two different morphologies: (1) straight, regular lamellae and (2) curved, irregular lamellae forming labyrinth-like structures.[9]

Thermo-mechanical processing (TMP) has shown the ability to modify the microstructure of the eutectic alloy.[5,10–12] TMP via cold rolling and subsequent annealing resulted in the lamellar breakdown and a microstructure with bimodal grain distribution.[13] Heterogeneous microstructure containing lamellar and nanocrystalline regions was observed in the alloy after hybrid rolling involving cryo- and warm rolling.[13] Apart from the various TMP techniques, strain paths adopted during TMP

(Received December 20, 2022; accepted May 25, 2023; published online June 21, 2023)

Table I. Elemental composition obtained from SEM and predicted by CALPHAD. $L1_2$-1, $L1_2$-2 and $L1_2$-3 correspond to proeutectic, irregular and regular $L1_2$, respectively

	Nominal eutectic composition	SEM EDS (n = 5)					CALPHAD					
							1353°C	1000°C		700°C		
		Overall	$L1_2$-1	$L1_2$-2	$L1_2$-3	B2	FCC	FCC	B2	FCC	σ	B2
Al	16.39	14.5 ± 1.7	7.4 ± 0.3	7.3 ± 0.8	9.1 ± 0.8	25.3 ± 1.9	11	6.6	24.4	2.9	0.0004	27.0
Co	16.39	16.8 ± 0.3	21.3 ± 0.4	21.4 ± 0.4	20.9 ± 0.6	13.1 ± 0.8	20	17.5	17.9	15.4	17.6	15.7
Cr	16.39	16.4 ± 1.4	20.5 ± 0.1	20.0 ± 0.4	19.3 ±	6.5 ± 0.6	18	22.1	8.2	24.7	57.8	7.2
Fe	16.39	16.7 ± 0.6	18.7 ± 0.3	18.4 ± 0.4	17.4 ± 0.5	10.6 ± 0.9	17	19.3	14.5	19.5	15.1	12.5
Ni	34.43	35.8 ± 0.3	32.1 ± 0.5	32.9 ± 0.3	33.5 ± 0.6	44.5 ± 0.7	34	34.5	34.9	37.5	9.5	37.5

also played a key role in defining the microstructure of the alloy.[11,14,15] Besides lamellar breakdown and grain refinement, TMP also resulted in the precipitation of Al-Ni-rich B2 within the FCC phase and Cr-rich coherent BCC nano-precipitates within the B2 phase.[3,7] Additionally, σ phase formation was reported within the recrystallized regions after TMP at 600°C.[16] Furthermore, TMP at and above 1000°C led to the disordering of the $L1_2$ phase.[10,12,17] However, $L1_2$ ordering was retained at and below 600°C.[8,16] These microstructural and phase transformations associated with TMP improved the mechanical behaviour of the eutectic alloy. The superior mechanical properties of the thermo-mechanically processed alloy were associated with the presence of semi-coherent second-phase particles and solid solution strengthening.[7] Apart from promising mechanical properties, the TMP alloy also exhibited excellent resistance to grain growth even at annealing temperatures as high as 0.91 of the melting point.[12,18]

Besides the eutectic composition, the microstructural evolution and mechanical behaviour of the near eutectic compositions of $AlCoCrFeNi_{2.1}$ were explored by Lozinko et al. and Joseph et al.[9,19]. When a lower Al and higher Ni percentage caused pro-eutectic $L1_2$ phase formation, higher Al and lower Ni resulted in a pro-eutectic B2.[9,19] The fraction of irregular eutectic colonies was reported to be higher in near eutectic compositions as opposed to the eutectic alloy.[7] Kim et al. further studied the effect of Ta on the microstructure and mechanical behaviour of the $AlCoCrFeNi_{2.1}$ alloy.[20,21] The increase in Ta and Al fraction beyond an optimum value was reported to retard the plasticity of the alloy.[21,22] Additionally, compared to the equiatomic and eutectic compositions, the near eutectic alloys displayed superior properties.[20,21] These studies are essential as maintaining the exact eutectic composition during large-scale synthesis can be challenging. Since the alloy with lower Al and higher Ni percentage displayed superior mechanical behaviour,[23] a near-eutectic alloy of similar composition was chosen for the present study. Though several studies exist on the effect of TMP on the microstructural morphology, precipitation and phase fraction, a systematic study on the effect of annealing duration on the microstructural changes is absent in the literature. Furthermore, the literature is predominantly focused on the microstructure and properties of the eutectic alloy. Thus, the current study aims to understand the effect of the pro-eutectic phase and annealing duration on lamellar and phase stability. The evolution of phases and microstructural morphology during solidification is also investigated. The work also explores the effect of heat treatment on the precipitation and mechanical behaviour of the alloy.

Table II. Elemental composition of phases after heat treatment obtained from SEM EDX.

Element↓ (n = 3)	1000°C−100 h		700°C−100 h	
	B2	FCC	B2	$L1_2$
Al	25.91 ± 0.76	4.85 ± 0.58	23.47 ± 1.03	5.12 ± 0.45
Co	11.14 ± 0.14	20.12 ± 0.63	10.04 ± 0.83	19.83 ± 0.39
Cr	3.43 ± 0.26	22.32 ± 0.21	3.10 ± 0.54	21.64 ± 0.77
Fe	9.37 ± 1.12	21.00 ± 0.18	8.53 ± 0.72	19.85 ± 0.87
Ni	50.17 ± 2.23	31.73 ± 1.32	45.52 ± 0.67	32.32 ± 0.95

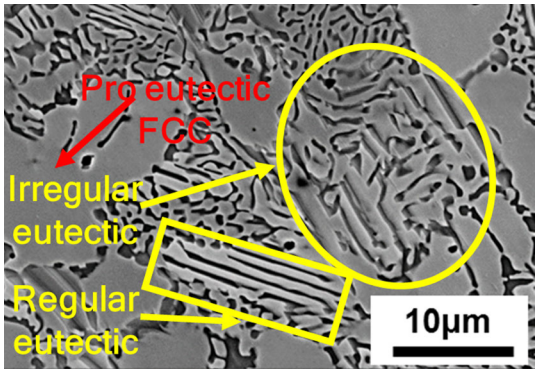

Fig. 1. SEM annular backscattered micrographs showing proeutectic, irregular eutectic and regular eutectic regions of the alloy.

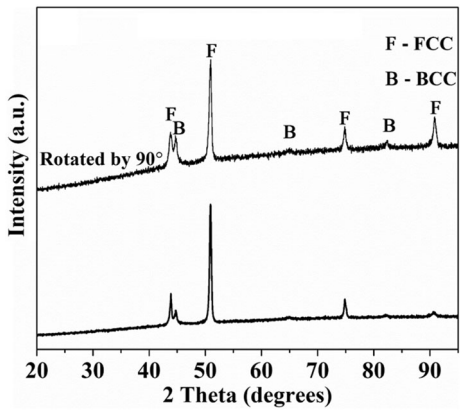

Fig. 2. XRD patterns of as-cast alloy.

EXPERIMENTAL AND COMPUTATIONAL METHODS

The alloy prepared by arc melting required proportions of Al, Co, Cr, Fe and Ni from elemental shots of 99.5% purity in a high vacuum system (8×10^{-5} mbar). A replaceable thoriated tungsten tip was used as the electrode. Before melting the above-mentioned elements, a Ti getter was melted to minimize the oxygen concentration within the arc melting chamber. For achieving superior chemical homogeneity, the arc melting system was equipped with a facility for electromagnetic stirring. The melt was chill cast into rods of 10 mm diameter and 100 mm height. From these rods, samples of 6.5 mm diameter and 3 mm height were obtained using electric discharge machining (EDM) for heat treatment studies. Similarly, for deformation studies, samples of 6.5 mm diameter and 10 mm height were machined.

To understand the phase stability and precipitation behaviour, the as-cast samples were heat-treated in a muffle furnace (INDFURR 1400°C) at 1000°C for 1 h, 24 h and 100 h, respectively. Additionally, heat treatment was done at 700°C for 100 h to study σ phase formation. Post-heat treatment, the samples were water quenched (WQ). To investigate the possibility of phase transformation at a lower cooling rate, a sample was heat-treated at 1000°C for 100 h and furnace-cooled (FC). Prior to heat treatment, the samples were vacuum sealed in quartz tubes to maintain an inert atmosphere.

A PANalytical X'Pert Pro x-ray diffractometer with CuKα radiation (wavelength – 0.154 nm) was employed to identify the phases and their lattice parameters. XRD was carried out at 45 kV and 30 mA, between 2θ angles of 20–90º with a step size of 0.02 and time per step of 20 s. The analysis was performed using the X'pert High Score Plus software with the database files. A Helios G4UX equipped with energy dispersive x-ray spectroscopy (EDS) was used to study the microstructural features and chemical composition of the alloy. Image J software was used for phase fraction quantification and lamellar thickness measurement (average of value from five SEM micrographs). Phase identification and local phase composition were investigated using Tecnai T20 transmission electron microscope (TEM) equipped with EDX detector from EDAX Instruments. CALPHAD (Calculation of Phase Diagram) studies were conducted using Thermo-Calc software in combination with the TCHEA2 database. Room temperature compression tests were carried out at a strain rate of 10^{-3} s^{-1} using Zwick/Roell Z100 universal testing machine, and the displacement was recorded with the aid of the Zwick video extensometer. The experiment was conducted again to confirm repeatability.

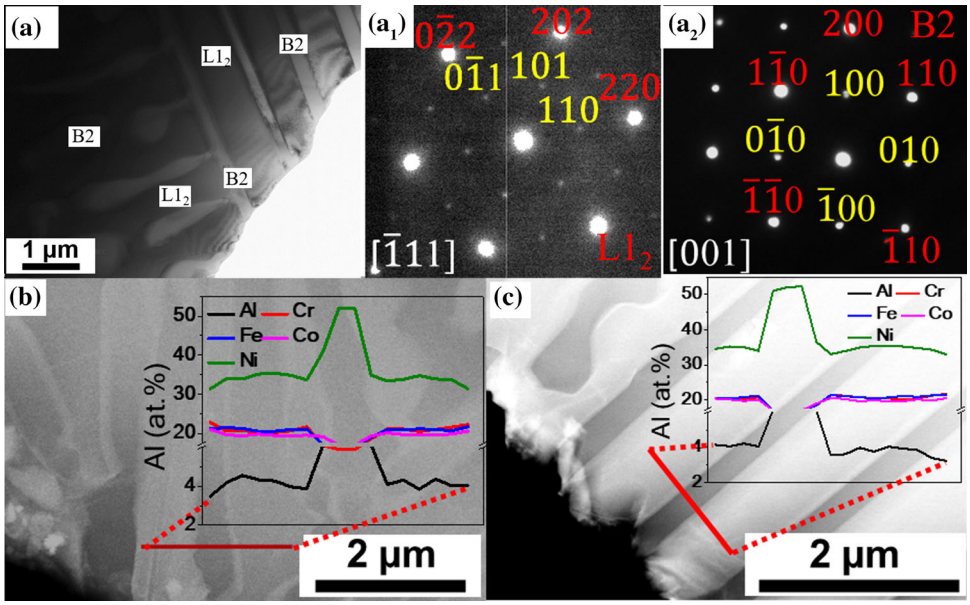

Fig. 3. (a) TEM bright-field micrographs showing the lamellar regions of $L1_2$ and B2, (a_1), (a_2) selected area diffraction patterns of B2 and $L1_2$, respectively, TEM bright-field micrographs from (b) irregular and (c) regular eutectic regions with composition along the red line.

RESULTS AND DISCUSSION

Microstructural Evolution of As-Cast Near Eutectic Alloy

The overall chemical composition of the alloy obtained by EDS displayed a lower Al and higher Ni percentage than the eutectic composition (Table I).[3] As expected, the SEM micrographs of the as-cast near eutectic alloy depicted a microstructure containing a eutectic mixture of $L1_2$ and B2 phase and a proeutectic $L1_2$ phase (Fig. 1). Based on the morphology, the microstructure was divided into three different regions: pro-eutectic $L1_2$, regular straight lamellar eutectic and irregular eutectic regions.

Solidification of the eutectic mixture starts with the growth of regular straight lamellae with weak anisotropic variations.[24] This regular eutectic formation is associated with the steady-state coupled growth of $L1_2$ and B2 phases from the liquid melt. As solidification progresses, instabilities leading to irregular eutectic growth can develop because of the variations in the concentration boundary layer ahead of the eutectic front. This results in the deviation from steady-state growth.[23] Partition of eutectic into regular and irregular regions can also occur because of temperature gradient and variation in cooling rate above and below a critical value.[25] The irregular eutectic formation is also associated with transverse phase diffusion and capillary effects leading to heterogeneity in interfacial energy and local chemical composition.[26,27] Atomistic facets implying heterogeneity in interfacial energy were reported in eutectic AlCoCrFeNi$_{2.1}$.[28] Apart from the formation of irregular eutectic structures, these can also lead to dynamic instabilities like lamellar elimination, zig-zag instability, and 1-λ or 2-λ instabilities (λ—interlamellar spacing).

Though reported to contain $L1_2$ and B2 phases in as-cast conditions, the superlattice reflections were not found in the XRD patterns of the present alloy (Fig. 2). However, these superlattice reflections were observed in the SAED pattern, confirming them to be $L1_2$ and B2, respectively (Fig. 3a_1 and a_2). The absence of superlattice peaks in XRD is due to the lower order parameter of $L1_2$ and B2 phases in the as-cast condition. The order parameter is lowered because of the supersaturation of $L1_2$ with Al and Ni, and B2 with Cr. This deviates the composition from their prototypical stoichiometry (NiAl for B2 and Ni_3Al for $L1_2$) and reduces the intensity of superlattice reflections. The variation in relative peak intensities (Fig. 2) upon rotating the sample is due to the crystallographic texture and the larger grain size, which limits diffraction to fewer grains. From XRD patterns using the Nelson–Riley function, the lattice parameters of the $L1_2$ and B2 phases were found to be 3.56 and 2.87 Å, respectively. Pang et al. and Duan et al. reported the $L1_2$ phase in as-cast condition to be a mixture of FCC with nanosized $L1_2$ precipitates.[29,30] These $L1_2$ precipitates were enriched in Al and Ni.[6] However, in the present study, such elemental segregation was not observed within the $L1_2$ phase in the as-cast condition. The precipitation observed in the works of Pang et al. and Dual et al. are attributed to the slow cooling rates associated with the adopted synthesis route. Solidification in these works took place in preheated ceramic crucibles, which results in slower cooling rates leading to prolonged high-temperature exposure.

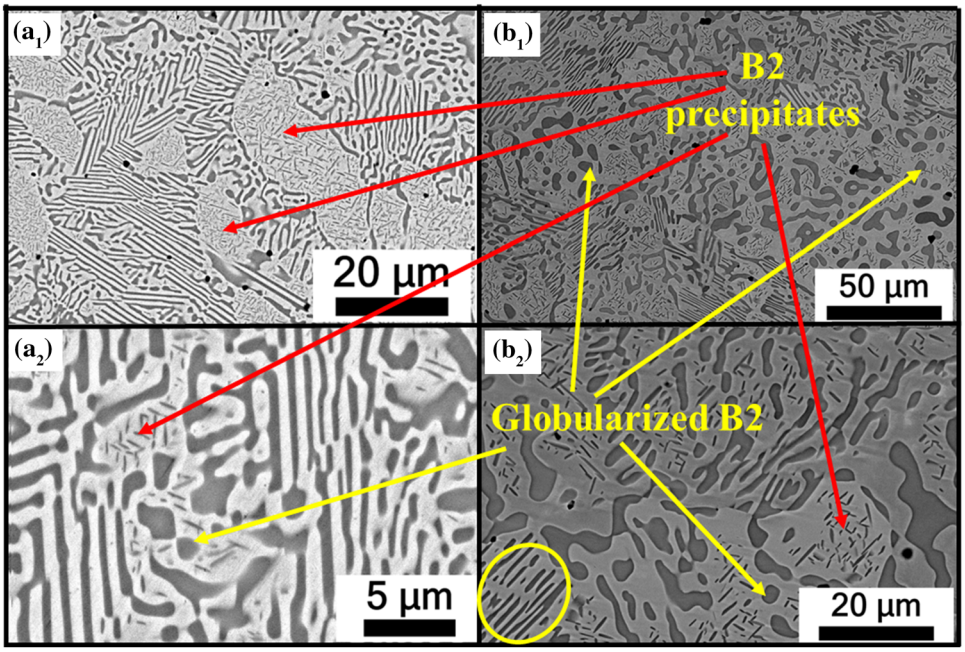

Fig. 4. SEM BSE micrographs of the alloy heat-treated at 1000°C for (a) 1 h and (b) 100 h. Subscripts 1 and 2 correspond to microstructure at lower and higher magnification.

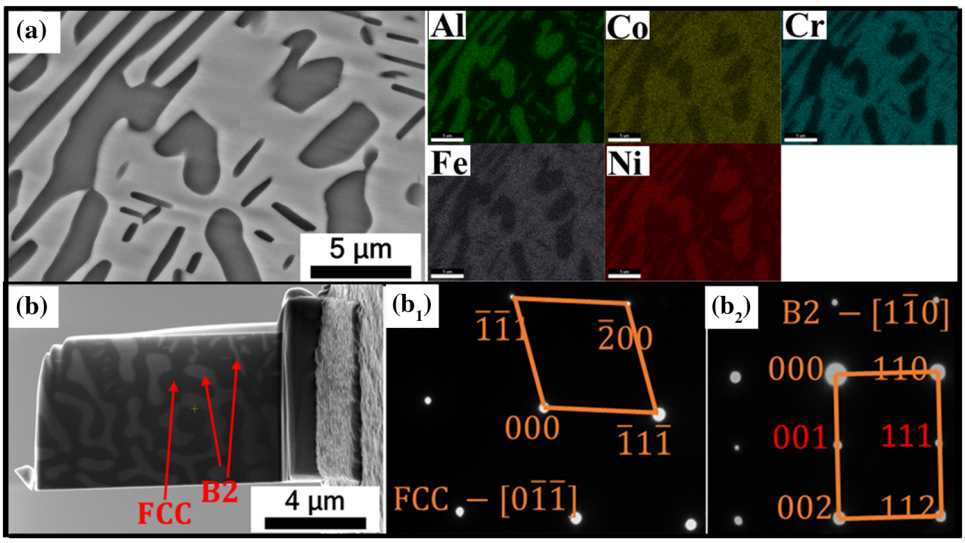

Fig. 5. (a) SEM EDX elemental mapping, (b) SEM micrograph of TEM lamella, selected area diffraction pattern of (b_1) FCC and (b_2) B2 of the alloy heat-treated at 1000°C for 100 h.

In line with the phase composition reported in the literature, the B2 phase was rich in Al and Ni, and $L1_2$ was Co-Cr-Fe-Ni rich (Table I).[3,10,31] TEM line EDS scan from the regular and irregular eutectic regions revealed larger chemical heterogeneity of Al and Ni within the $L1_2$ phase of irregular eutectic regions (Fig. 3b, c). Furthermore, the phase fraction of the $L1_2$ and B2 phases was found to be 79% and 21%, respectively. Within the regular eutectic region, the lamellar thickness of $L1_2$ and B2 lamellae was 1.25 ± 0.31 and 0.64 ± 0.16 μm, while in irregular regions, it was 0.53 ± 0.32 and 0.8 ± 0.23 μm, respectively.

Thermal Stability of the Alloy

Heat treatment at 1000°C for various durations resulted in precipitates of acicular morphology homogeneously distributed within the pro-eutectic and irregular eutectic regions (Fig. 4a_1, b_1 and b_2). Interestingly, the regular lamellar regions were

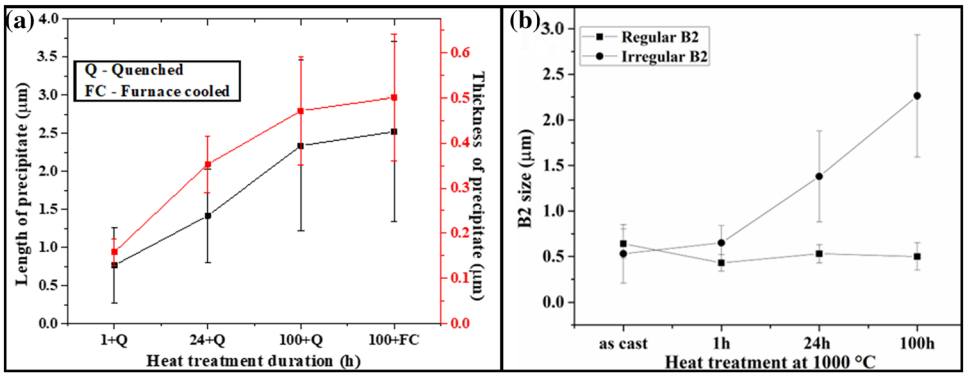

Fig. 6. (a) Variation of B2 precipitate size, (b) variation of B2 lamellar size with annealing time after 1000°C heat treatment (the lines in the figures are for representative purpose and does not imply the trend between the duration).

devoid of these precipitates (Fig. 4b$_2$). These precipitates rich in Al and Ni (Fig. 5a) displayed superlattice reflections and were found to be B2 (Fig. 5b$_2$). The acicular morphology of the Al-Ni-rich precipitates could be due to anisotropic interfacial and elastic strain energies associated with the multi-component matrix. Anisotropic elastic energies create elastically hard and soft directions resulting in precipitates aligning to elastically soft directions.[32] As Fig. 5a shows, the B2 precipitates were oriented in specific preferred crystallographic directions. Apart from the elastic energy, the anisotropy of interfacial energies between precipitate and matrix can also contribute to acicular morphology.[28,33]

After 1 h of heat treatment, the dimensions (length: thickness) of the precipitates were 0.76 ± 0.49 and 0.16 ± 0.03 μm, respectively, which further increased with annealing duration (Fig. 6a). Though the precipitate size increased, the acicular morphology of the precipitates was retained even after 100 h of heat treatment. The microstructure of 1000°C–100 h condition was similar after both quenching and furnace cooling. When the precipitate size (length and thickness) of quenched sample was 2.34 ± 1.12 and 0.47 ± 0.12 μm (aspect ratio = 5), the size of the furnace cooled sample was 2.52 ± 1.18 and 0.50 ± 0.14 μm (aspect ratio = 5), respectively. The SAED pattern associated with the L1$_2$ phase after 1000°C heat treatment was devoid of superlattice reflections, indicating the disordering of the phase (Fig. 5b$_1$).

Apart from L1$_2$ disordering, thermal exposure also resulted in lamellar instability leading to coarsening and globularization of the B2 phase within the irregular eutectic region (Fig. 4a$_2$, b$_1$ and b$_2$). The extent of coarsening and globularization of irregular eutectic regions increased with annealing duration (Fig. 4a$_1$, b$_1$). However, the B2 lamellar thickness in regular eutectic regions was almost independent of annealing time (Fig. 6b). This can be due to the difference in FCC-B2 interfacial energy associated with regular and irregular eutectic regions. Unlike the irregular regions, the regular eutectic regions formed via steady-state coupled growth are presumed to have uniform interfacial energy.[34] Furthermore, the limited chemical heterogeneity within the regular eutectic region creates a minimum concentration gradient within the phases (Fig. 3c). This leads to slower coarsening and globularization kinetics of B2 within the regular eutectic regions. Though the kinetics of globularization was slower in the regular eutectic region, after 100 h of heat treatment, the breakage of B2 lamellae was observed (encircled in Fig. 4b$_2$).

As in 1000°C heat-treated alloy (Fig. 4), thermal exposure at 700°C for 100 h also led to Al-Ni-rich acicular B2 precipitates confined to pro-eutectic and irregular eutectic regions (Fig. 7a, b). These precipitates were significantly finer than those at 1000°C and exhibited dimensions (length: thickness) of 0.66 ± 0.27 and 0.06 ± 0.02 μm (aspect ratio = 11). Furthermore, heat treatment at 700°C resulted in localized globularization of the B2 phase within the irregular eutectic regions (inset images in Fig. 7a). However, the L1$_2$ phase ordering was retained after 100 h of thermal exposure at 700°C (Fig. 7c1). Thus, the L1$_2$ phase can be concluded to undergo sequential ordering (i.e., order–disorder transformation below the melting point) between 700°C and 1000°C. The addition of Fe to the L1$_2$ phase containing Ni and Al (Ni$_3$Al) has been reported to transform ordering from direct to sequential.[35,36] In this alloy, multiple elements like Fe, Co and Cr can be presumed to have lowered the order transition temperature. Apart from B2 precipitation within the L1$_2$ phase, heat treatment at 700°C displayed Cr-rich nanoprecipitates within the lamellar B2 phase (Fig. 7c2). Similar Cr-rich precipitates were found after TMP at 600°C and were reported to be BCC.[6]

Based on the overall chemical composition obtained from SEM-EDS (Table I), stable phases and their composition at various temperatures were determined using CALPHAD method. The primary phase to solidify from liquid was predicted to be an

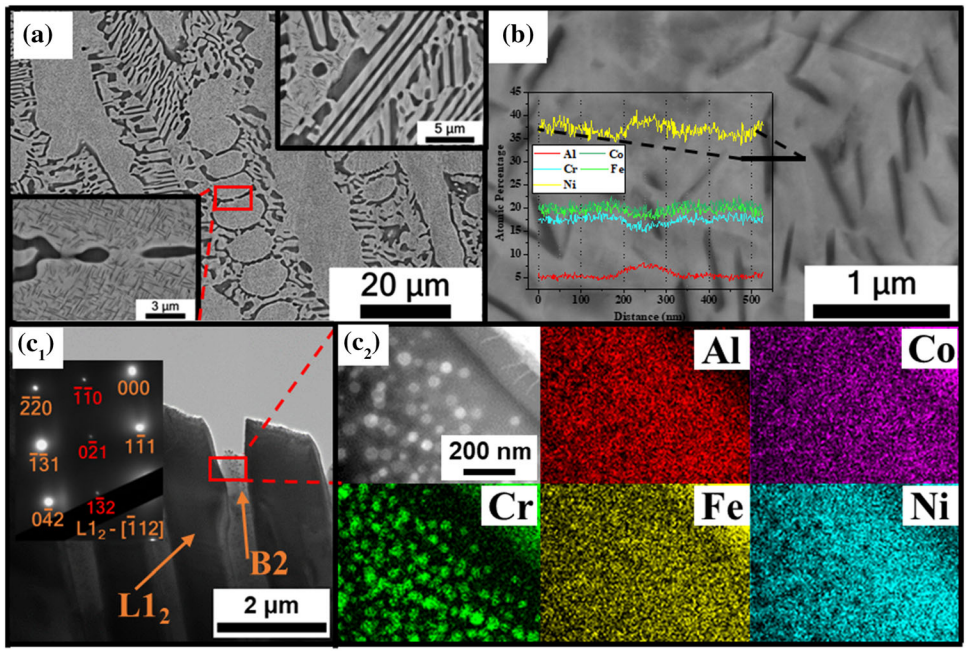

Fig. 7. (a) SEM BSE micrographs of the alloy heat-treated at 700°C for 100 h, (b) line scan confirming the acicular precipitate to be Al-Ni type, (c_1) TEM bright-field micrograph and selected area diffraction pattern of $L1_2$ and (c_2) elemental mapping from B2 region displaying Cr-rich nano-precipitates within the B2 matrix.

FCC phase at 1353°C. The chemical composition of this FCC phase was similar to the proeutectic $L1_2$ of as-cast alloy (Table I). Furthermore, the eutectic temperature resulting in liquid to FCC and B2 transformation was found to be 1330°C, and these eutectic phases were predicted to be stable up to 1000°C. The B2 was enriched in Al and Ni, and FCC Cr-Fe rich (Table I). CALPHAD studies on the FCC phase displayed a decrease in Al and Co and an increase in Cr and Fe percentage with a decrease in temperature (Table I). Furthermore, the supersaturation of Al in $L1_2$ of cast alloy was confirmed by comparing phase compositions of as-cast $L1_2$ to those predicted by CALPHAD at 1000 and 700°C (Table I).

To further understand the order–disorder transformation between FCC and $L1_2$, another series of CALPHAD studies was conducted. In these calculations, the compositions of the FCC phase at 1000°C and the $L1_2$ phase at 700°C were considered as overall compositions. All the phases except FCC and $L1_2$ were suspended. At 1000°C, FCC was found to be the only stable phase for both compositions. However, at 700°C, $L1_2$ appears as a stable phase along with the FCC phase. This result supports the experimental observation of ordering transformation between 1000°C and 700°C discussed earlier. Furthermore, by comparing CALPHAD and experimental data, it can be concluded that the alloy, during solidification, crystallizes as FCC from the liquid state and undergoes sequential ordering at a temperature between 700°C and 1000°C.

From CALPHAD studies at 700°C, apart from FCC and B2, a minor fraction of Cr-rich σ phase formation was also expected. σ Phase formation has also been reported in thermo-mechanically processed eutectic alloy.[16] However, in the present work, the σ phase was not observed after thermal exposure at 700°C for the following reasons. The driving force (151 J/mol) for σ formation in the present alloy was lower than that in the eutectic alloy (352 J/mol). CALPHAD studies also reveal that the equilibrium amount of the σ phase reduced from 7.2% in eutectic alloy to 6.6% in the present alloy. Furthermore, the kinetic assistance available for σ formation during the TMP is absent in the present case.

Heat treatment reduced the Al content in $L1_2$/FCC and Cr content in B2 (Table II). This decrease in Al after heat treatment is associated with the precipitation of B2 from supersaturated $L1_2$. Table I shows the supersaturation of various $L1_2$ regions with Al, Co and Ni in as-cast alloy compared to that predicted by CALPHAD at 1000°C. Interestingly, albeit having a higher degree of supersaturation, the regular $L1_2$ phase was devoid of precipitates. CALPHAD studies at 1000°C for specific compositions of regular and irregular $L1_2$ (from Table I) revealed the former to have lower Gibbs energy (− 85 kJ/mol) than the latter (− 83.4 kJ/mol). Thus, compared to the irregular $L1_2$, the regular $L1_2$ is expected to have higher stability and lower tendency for phase decomposition.

He et al.[37] reported FCC phase decomposition owing to severe lattice distortions in Co-Cr-Fe-Ni systems. They also proved that minor additions of elements like Al having larger atomic size could accelerate this decomposition process. Thus, the $L1_2$

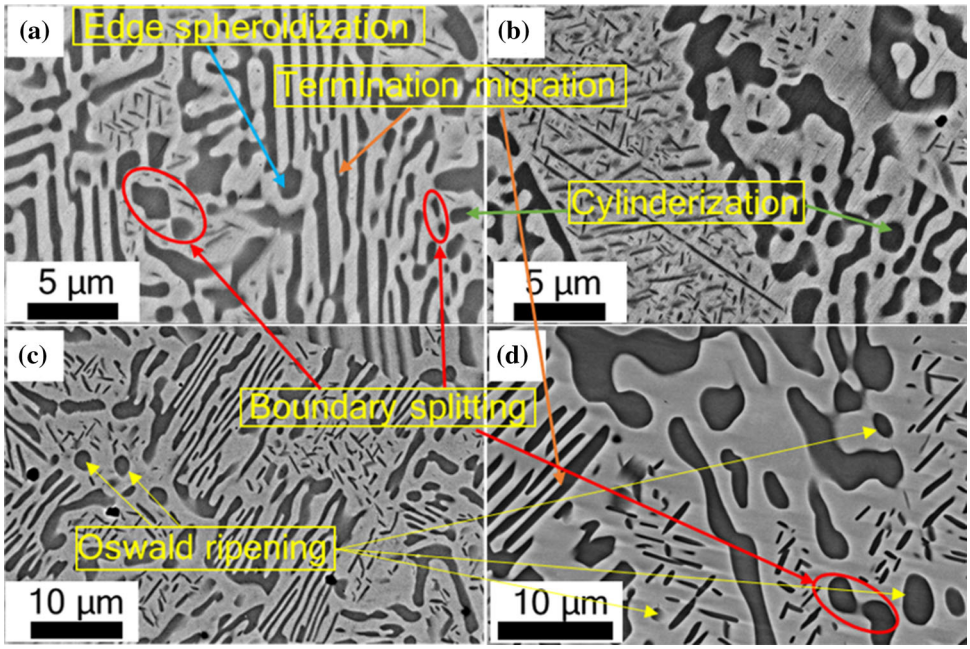

Fig. 8. SEM annular BSE micrographs of the alloy heat-treated at 1000°C for (a), (b) 1 h, (c) 24 h, (d) 100 h.

phase of the present alloy containing Al, Co, Cr, Fe and Ni is expected to have a driving force for phase decomposition. However, compared to regular $L1_2$, the higher order of chemical heterogeneity observed in irregular $L1_2$ (Fig. 3b) can result in non-uniform lattice strain. Furthermore, the lattice strain energy within the regular eutectic is expected to be lower because of steady-state coupled growth. This can retard the kinetics of phase decomposition within the regular $L1_2$. Thus, despite supersaturation, higher stability and reduced lattice strain associated with regular $L1_2$ can retard its phase decomposition compared to irregular $L1_2$.

The lamellar degradation during annealing has been attributed to mechanisms like termination migration, globularization and cusping.[8] Phenomena like the minimization of interfacial energy and capillary forces have been ascribed as the driving force behind these mechanisms.[8] In the current alloy, mechanisms like cylinderization and edge spheroidization were observed to dominate during the initial stages of globularization (1 h of heat treatment) (Fig. 8a, b). With the increase in annealing time, termination migrations and boundary splitting were also observed (Fig. 8c, d). At longer annealing durations, the globularized B2 phase underwent Ostwald ripening, which can be linked to the minimization of interfacial energy.[8]

The FCC: B2 phase vol.% changed to 64:36 after 1 h of heat treatment at 1000°C compared to that in as-cast condition (79:21). Interestingly, the precipitate fraction decreased with an increase in heat treatment duration, while the overall B2 phase fraction remained constant (~35%) (Fig. 9a). The decrease in precipitate fraction with annealing time is attributed to globularization and Ostwald ripening. A phase fraction after 700°C heat treatment was identical to that after 1000°C (Fig. 9a). This overall phase fraction was similar to that of the eutectic alloy.[12] Thus, it can be concluded that heat treatment duration and the current temperature range (700–1000°C) do not influence the overall B2 phase fraction.

Room Temperature Compressive Deformation Behaviour

The yield strength of the alloy increased from 524 MPa to 600 MPa upon thermal exposure (Fig. 9-b). However, Young's modulus was found to be 103 GPa before and after heat treatment. The yield strength of the near eutectic alloy was well within the range reported for eutectic alloys in the literature.[4–6,10,16,37–39] The increase in yield strength without TMP, and merely by heat treatment, is attributed to the homogeneous precipitation of the hard B2 phase within relatively softer pro-eutectic and irregular eutectic FCC/$L1_2$ region. These precipitates constrain the plastic deformation of the soft FCC/$L1_2$ phase, thereby introducing long-range back stresses. Shi et al. have shown the influence of back stress in enhancing the yield strength of thermo-mechanically processed alloy.[5] Compared to as-cast alloy, the presence of precipitates in TMP alloy increased the back stress associated with the FCC phase, which improved the global yield strength of the alloy.[5] However, despite identical phase fraction, the yield strength of the heat-treated alloy was inferior to the TMP eutectic alloy reported in the literature.[5,6,10,12,16,37,39,40] This inferior strength can be attributed to the fine grain size,

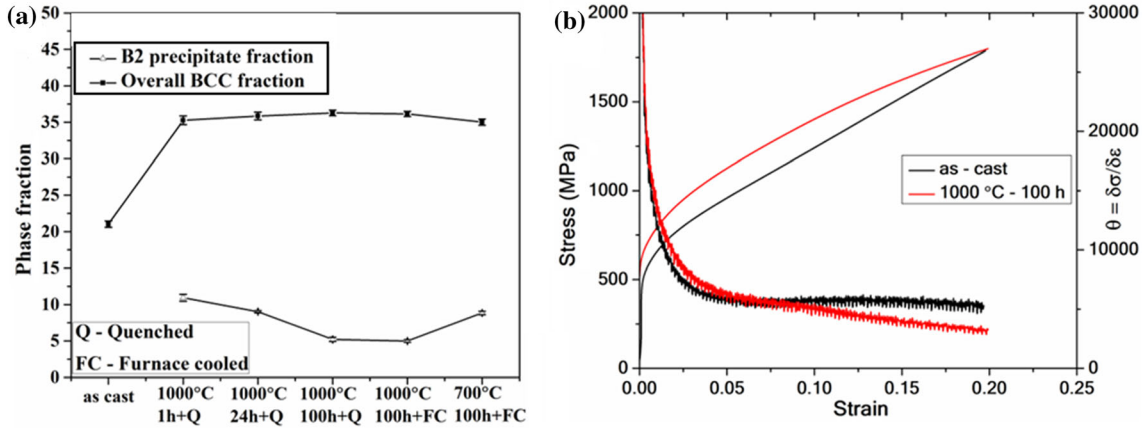

Fig. 9. (a) Variation of B2 phase fraction with heat treatment condition (the lines in the figure are for representative purpose and does not imply the trend between the duration) and (b) room temperature true stress-strain and work hardening curves of as-cast and heat-treated alloy.

twins and intergranular B2 precipitation in the thermo-mechanically processed alloy.[5,41]

The work-hardening behaviour of the as-cast and heat-treated alloys was similar during the initial stages of deformation (Fig. 9b). The B2 phase in Al-Co-Cr-Fe-Ni alloy system has been reported to exhibit a superior strength than the FCC phase.[42] Furthermore, $L1_2$ phase can effectively accommodate higher fractions of plastic strains, thereby enhancing plasticity.[20,21] Hence, during the initial stages of straining, the FCC phase undergoes deformation prior to the B2. This leads to similar work hardening behaviour in both as-cast and heat-treated alloys.

However, during the later stages, the as-cast alloy exhibited a superior work hardening rate. The inferior work hardening rate in the later stages of deformation can be attributed to the coarsening and globularization of the B2 phase upon heat treatment. This relieves the constraints associated with the FCC phase, reducing the back stress developed within the phase. Nevertheless, the strength-ductility synergy is expected to be superior post-heat treatment because of the breakdown of long lamellae, which otherwise can act as crack propagation sites. Additionally, the precipitation fine B2 phase can strengthen the alloy via Orowan mechanism.[21]

CONCLUSION

- The alloy was found to solidify as FCC and later undergo sequential ordering to $L1_2$ at transition temperatures between 700°C and 1000°C.
- Heat treatment resulted in localized globularization of B2 due to lamellar instability. Furthermore, homogeneous precipitation of acicular B2 occurred within the proeutectic and irregular eutectic regions. Supersaturation of Al and superior stability of regular $L1_2$ were found to influence the B2 precipitation.
- The precipitation increased the overall B2 phase fraction of the alloy to that reported for eutectic composition. Heat treatment temperature and duration displayed minimal effect on the overall B2 fraction. However, the precipitate fraction decreased with an increase in annealing time.
- The homogeneous B2 precipitation upon thermal exposure enhanced the mechanical behaviour of the alloy. However, the work hardenability was found to be superior for as-cast alloy.

ACKNOWLEDGEMENT

The authors would like to acknowledge Dr. M. Nagini for her help in TEM characterization.

FUNDING

Open Access funding enabled and organized by CAUL and its Member Institutions.

DATA AND CODE AVAILABILITY

Not applicable.

CONFLICT OF INTEREST

On behalf of all authors, the corresponding author states that there is no conflict of interest.

ETHICAL APPROVAL

Not applicable.

REFERENCES

1. D.B. Miracle and O.N. Senkov, *Acta Mater.* 122, 448 https://doi.org/10.1016/j.actamat.2016.08.081 (2017).
2. B.S. Murty, J.W. Yeh, S. Ranganathan, and P.P. Bhattacharjee, *High-entropy alloys* (Elsevier, Amsterdam, 2019), p388.
3. Y. Lu, Y. Dong, S. Guo, L. Jiang, H. Kang, T. Wang, B. Wen, Z. Wang, J. Jie, Z. Cao, H. Ruan, and T. Li, *Sci. Rep.* 4, 6200 https://doi.org/10.1038/srep06200 (2014).
4. I.S. Wani, T. Bhattacharjee, S. Sheikh, Y. Lu, S. Chatterjee, S. Guo, P.P. Bhattacharjee, and N. Tsuji, in *IOP Conference Series: Materials Science and Engineering*, vol. 194 (2017). https://doi.org/10.1088/1757-899x/194/1/012018.
5. P. Shi, W. Ren, T. Zheng, Z. Ren, X. Hou, J. Peng, P. Hu, Y. Gao, Y. Zhong, and P.K. Liaw, *Nat. Commun.* 10, 489 https://doi.org/10.1038/s41467-019-08460-2 (2019).
6. T. Xiong, S. Zheng, J. Pang, and X. Ma, *Scripta Mater.* 186, 336–340 https://doi.org/10.1016/j.scriptamat.2020.04.035 (2020).
7. X. Gao, Y. Lu, B. Zhang, N. Liang, G. Wu, G. Sha, J. Liu, and Y. Zhao, *Acta Mater.* 141, 59–66 https://doi.org/10.1016/j.actamat.2017.07.041 (2017).
8. L. Wang, X. Wu, C. Yao, J. Shen, Y. Zhang, Y. Ge, and G. Zhang, *Metall. Mater. Trans. A.* 51, 5781 https://doi.org/10.1007/s11661-020-05993-w (2020).
9. A. Lozinko, Y. Zhang, O.V. Mishin, U. Klement, and S. Guo, *J. Alloys Compd.* 822, 153558 https://doi.org/10.1016/j.jallcom.2019.153558 (2020).
10. T. Bhattacharjee, I.S. Wani, S. Sheikh, I.T. Clark, T. Okawa, S. Guo, P.P. Bhattacharjee, and N. Tsuji, *Sci. Rep.* 8, 3276 https://doi.org/10.1038/s41598-018-21385-y (2018).
11. A. Patel, I. Wani, S.R. Reddy, S. Narayanaswamy, A. Lozinko, R. Saha, S. Guo, and P.P. Bhattacharjee, *Intermetallics* 97, 12–21 https://doi.org/10.1016/j.intermet.2018.03.007 (2018).
12. I.S. Wani, T. Bhattacharjee, S. Sheikh, P.P. Bhattacharjee, S. Guo, and N. Tsuji, *Mater. Sci. Eng. A* 675, 99–109 https://doi.org/10.1016/j.msea.2016.08.048 (2016).
13. A.E. Afolabi, A.P.I. Popoola, and O.M. Popoola, in *Handbook of Nanomaterials and Nanocomposites for Energy and Environmental Applications*, (2020), pp 1–27.
14. S.R. Reddy, U. Sunkari, A. Lozinko, S. Guo, and P.P. Bhattacharjee, *J. Mater. Res.* 34, 687–699 https://doi.org/10.1557/jmr.2018.409 (2019).
15. S.R. Reddy, U. Sunkari, A. Lozinko, S. Guo, and P.P. Bhattacharjee, in *Journal of physics: conference series*, vol 1270 (2019). https://doi.org/10.1088/1742-6596/1270/1/012054.
16. S.R. Reddy, S. Yoshida, U. Sunkari, A. Lozinko, J. Joseph, R. Saha, D. Fabijanic, S. Guo, P.P. Bhattacharjee, and N. Tsuji, *Mater. Sci. Eng. A* 764, 138226 https://doi.org/10.1016/j.msea.2019.138226 (2019).
17. M.H. Asoushe, A.Z. Hanzaki, H.R. Abedi, B. Mirshekari, T. Wegener, S.V. Sajadifar, and T. Niendorf, *Mater. Sci. Eng. A* 799, 140012 https://doi.org/10.1016/j.msea.2020.140012 (2021).
18. I.S. Wani, T. Bhattacharjee, S. Sheikh, Y.P. Lu, S. Chatterjee, P.P. Bhattacharjee, S. Guo, and N. Tsuji, *Mater. Res. Lett.* 4, 174 https://doi.org/10.1080/21663831.2016.1160451 (2016).
19. J. Joseph, M. Imran, P.D. Hodgson, M.R. Barnett, and D.M. Fabijanic, *Manuf. Lett.* 25, 16 https://doi.org/10.1016/j.mfglet.2020.06.002 (2020).
20. M.J. Kim, G.C. Kang, S.H. Hong, H.J. Park, S.C. Mun, G. Song, and K.B. Kim, *J. Mater. Sci. Technol.* 57, 131 https://doi.org/10.1016/j.jmst.2020.03.045 (2020).
21. M.J. Kim, J.T. Kim, J. Elyorjon, G. Chan Kang, S.J. Hong, G. Song, J.K. Lee, J.H. Lee, and K.B. Kim, *Compos. Part B Eng.* 214, 108750 https://doi.org/10.1016/j.compositesb.2021.108750 (2021).
22. J.W. Choi, J.T. Kim, S.H. Hong, H.J. Park, E. Jumaev, and K.B. Kim, *J. Alloys Compd.* 933, 167679 https://doi.org/10.1016/j.jallcom.2022.167679 (2023).
23. Q. Wang, Y. Lu, Q. Yu, and Z. Zhang, *Sci. Rep.* 8, 14910 https://doi.org/10.1038/s41598-018-33330-0 (2018).
24. S. Bottin-Rousseau, M. Şerefoğlu, S. Yücetürk, G. Faivre, and S. Akamatsu, *Acta Mater.* 109, 259 https://doi.org/10.1016/j.actamat.2016.01.065 (2016).
25. D.I. Popov, L.L. Regel, and W.R. Wilcox, *Cryst. Growth Des.* 1, 313 https://doi.org/10.1021/cg005538v (2001).
26. M. Paul, *Dissipative structures and weak turbulence* (Springer, Berlin, Heidelberg, 1995).
27. A. Parisi, *Acta Mater.* 56, 1348 https://doi.org/10.1016/j.actamat.2007.11.037 (2008).
28. T. Xiong, W. Yang, S. Zheng, Z. Liu, Y. Lu, R. Zhang, Y. Zhou, X. Shao, B. Zhang, J. Wang, F. Yin, P.K. Liaw, and X. Ma, *J. Mater. Sci. Technol.* 65, 216 https://doi.org/10.1016/j.jmst.2020.04.073 (2021).
29. J. Pang, T. Xiong, W. Yang, H. Ge, X. Zheng, M. Song, H. Zhang, and S. Zheng, *J. Mater. Sci. Technol.* 129, 87 https://doi.org/10.1016/j.jmst.2022.04.023 (2022).
30. X. Duan, T. Han, X. Guan, Y. Wang, H. Su, K. Ming, J. Wang, and S. Zheng, *J. Mater. Sci. Technol.* 136, 97 https://doi.org/10.1016/j.jmst.2022.07.023 (2023).
31. T. Bhattacharjee, R. Zheng, Y. Chong, S. Sheikh, S. Guo, I.T. Clark, T. Okawa, I.S. Wani, P.P. Bhattacharjee, A. Shibata, and N. Tsuji, *Mater. Chem. Phys.* 210, 207 https://doi.org/10.1016/j.matchemphys.2017.06.023 (2018).
32. H. Mao, Y. Kong, D. Cai, M. Yang, Y. Peng, Y. Zeng, G. Zhang, X. Shuai, Q. Huang, K. Li, H. Zapolsky, and Y. Du, *Comput. Mater. Sci.* 184, 109878 https://doi.org/10.1016/j.commatsci.2020.109878 (2020).
33. V. Vaithyanathan, C. Wolverton, and L.Q. Chen, *Acta Mater.* 52, 2973 https://doi.org/10.1016/j.actamat.2004.03.001 (2004).
34. A. Karma, and A. Sarkissian, *Metall. Mater. Trans. A.* 27, 635 https://doi.org/10.1007/bf02648952 (1996).
35. R.W. Cahn, P.A. Siemers, J.E. Geiger, and P. Bardhan, *Acta Metall.* 35, 2737 https://doi.org/10.1016/0001-6160(87)90273-2 (1987).
36. R.W. Cahn, P.A. Siemers, and E.L. Hall, *Acta Metall.* 35, 2753 https://doi.org/10.1016/0001-6160(87)90274-4 (1987).
37. L. Wang, C. Yao, J. Shen, Y. Zhang, T. Wang, Y. Ge, L. Gao, and G. Zhang, *Intermetallics* 118, 106681 https://doi.org/10.1016/j.intermet.2019.106681 (2020).
38. X. Huang, Y. Hu, Z.T. Wu, Y. Dong, C.Q. Li, Y.Q. Cheng, and Z.R. Zhang, *Mater. Sci. Forum* 993, 281 https://doi.org/10.4028/www.scientific.net/MSF.993.281 (2020).
39. X. Hu and D. Chen, *J. Mater. Eng. Perform.* 27, 3566 https://doi.org/10.1007/s11665-018-3430-7 (2018).
40. S.R. Reddy, U. Sunkari, A. Lozinko, R. Saha, S. Guo, and P.P. Bhattacharjee, *Intermetallics* 114, 106601 https://doi.org/10.1016/j.intermet.2019.106601 (2019).
41. P. Shi, Y. Zhong, Y. Li, W. Ren, T. Zheng, Z. Shen, B. Yang, J. Peng, P. Hu, Y. Zhang, P.K. Liaw, and Y. Zhu, *Mater. Today* 41, 62 https://doi.org/10.1016/j.mattod.2020.09.029 (2020).
42. A.M. Giwa, P.K. Liaw, K.A. Dahmen, and J.R. Greer, *Extreme Mech. Lett.* 8, 220 https://doi.org/10.1016/j.eml.2016.04.013 (2016).